

Biases of PIV measurement of turbulent flow and the masked correlation-based interrogation algorithm

L. Gui, J. Longo, F. Stern

Abstract Influences of evaluation bias of the correlation-based interrogation algorithm on particle image velocimetry (PIV) measurement of turbulent flow are investigated. Experimental tests in the Iowa Institute of Hydraulic Research towing tank with a towed PIV system and a surface-piercing flat plate and simulations demonstrate that the experimentally determined mean velocity and Reynolds stress components are affected by the evaluation bias and the gradient of the evaluation bias, respectively. The evaluation bias and gradient of the evaluation bias can both be minimized effectively by using Gaussian digital masks on the interrogation window, so that the measurement uncertainty can be reduced.

1 Introduction

The correlation-based interrogation algorithm is the most commonly used technique for evaluating digital recordings in particle image velocimetry (PIV) experiments (Cenedese and Paglialunga 1990; Adrian 1991). Because it can be combined with the fast Fourier transformation (FFT) technique to accelerate the evaluation of PIV recordings, the correlation-based interrogation algorithm is frequently chosen for the study of turbulent flows (Liu et al. 1991; Schlueter and Merzkirch 1996; Westerweel et al. 1996; Xiong and Merzkirch 1997). Currently, it appears to be the best choice for building dedicated processors for virtually real-time display of PIV measurements, e.g., DANTEC FlowMap PIV 2000 processor. However, the application of the FFT requires the assumption that the functions to be correlated are distributed periodically. Because of this assumption, an evaluation bias is produced, and the total evaluation error (bias and random) depends directly on the particle image displacement (Willert and Gharib 1991; Westerweel 1997; Raffel et al. 1997). When using PIV systems for measuring the mean velocity of turbulent

flows, significant measurement biases are often observed (Freek et al. 1996, 1999), and the evaluation bias may be the primary bias error source (Gui et al. 1999).

To avoid the above disadvantage of the correlation-based interrogation algorithm, new algorithms based on the tracking of ensembles of particle images have been developed, e.g., the correlation-based tracking algorithm (Huang et al. 1993; Kemmerich and Rath 1994; Fincham and Spedding 1997) and the minimum quadratic difference (MQD) method (Gui and Merzkirch 1996, 2000). When using the tracking-based evaluation algorithms, there is no evaluation bias and the random evaluation error does not directly depend on the particle image displacement. Although the two methods can also be accelerated by using the FFT technique (Gui et al. 1998; Ronneberger et al. 1998), the evaluation speed is still much lower than that of the correlation-based interrogation algorithm and not high enough for rapid measurement and study of turbulent flows in many cases. The correlation-based interrogation algorithm is still widely used, but new techniques have been added for improving its performance. For instance, a window-offset technique is often used with the correlation-based interrogation algorithm for artificially reducing the particle image displacement to be determined by the algorithm, so that large evaluation errors can be avoided (Willert 1996). If the window offset is determined by the discrete part of the particle image displacement with one or more trial (previous) evaluations, the particle image displacement to be determined may be within 0.5 pixel, and very high evaluation accuracy can be achieved (Westerweel et al. 1997). However, it is not always possible to set window offsets optimally for all evaluation points in a PIV recording, and it is currently not practicable to do the trial evaluations for the turbulent measurements where a great number of PIV recordings should be taken and evaluated in a short time. Furthermore, in some cases, only one window offset can be chosen for a given measurement area of a PIV recording to avoid excessive particle image displacements, e.g., when using the DANTEC FlowMap 2000 processor in the IIHR towing tank. Fortunately, another technique, i.e., the window mask, can be used for further improvement of the correlation-based interrogation algorithm.

The idea of using a window mask to improve the correlation-based interrogation algorithm is not new (see Adrian 1988; Westerweel 1997). When applied to a pair of digitized PIV recording samples, which are described by gray value distributions $g_1(i, j)$ and $g_2(i, j)$ in a fixed interrogation window measuring $M \times N$ pixels, the evalua-

Received: 16 September 1999/Accepted: 7 February 2000

L. Gui (✉), J. Longo, F. Stern
Iowa Institute of Hydraulic Research (IIHR)
The University of Iowa
Iowa City, IA 52242, USA

This research was sponsored by the Office of Naval Research under Grant N000 14-96-0018 administered by Dr. E. P. Rood.

tion functions of the masked correlation interrogation algorithm can be written as

$$\Phi_1(m, n) = \sum_{i=1}^M \sum_{j=1}^N \omega(i, j) \cdot g_1(i, j) \times \omega(i + m, j + n) \cdot g_2(i + m, j + n) \quad (1)$$

The window mask $\omega(i, j)$ can be given as a Gaussian (exponential) function

$$\omega(i, j) = e^{-2 \left(\frac{(i-M/2)^2}{(M/2)^2} + \frac{(j-N/2)^2}{(N/2)^2} \right)} \quad (2)$$

The window mask technique described in Eq. (1) is only effective when the particle image displacement is relatively small (e.g., <5 pixels with a 32×32 -pixel interrogation window), which explains why it was not widely used before the technique of the window offset was developed. In order to increase the dynamic range of the mask technique, another evaluation function is suggested by Gui et al. (2000)

$$\Phi_2(m, n) = \sum_{i=1}^M \sum_{j=1}^N \omega(i, j)^2 \cdot g_1(i, j) \cdot g_2(i + m, j + n) \quad (3)$$

For this study, the masked correlation-based interrogation algorithm (with Φ_1 and Φ_2) is discussed after application to experimental turbulent flow measurements in the wake of a vertical surface-piercing flat plate in the Iowa Institute of Hydraulic Research (IIHR) towing tank and simulations. The experiments and simulations are used to evaluate the interrogation algorithm performance, quantify the evaluation bias uncertainty and its contribution to the total measurement uncertainty for mean and turbulent measurements, and provide insight for reducing measurement uncertainty in future PIV towing tank tests.

2

Experimental and simulation background

The experiments are conducted in the IIHR towing tank with a towed PIV system designed and manufactured by DANTEC Measurement Technology, see Gui et al. (1999). The PIV system contains a 20 mJ, dual cavity Nd:Yag laser and a cross-correlation camera with a digital resolution of $1,008 \times 1,018$ pixels. The camera is fitted with a $f/1.4$ 50 mm lens that views the light sheet from a distance of about 50 cm. The measurement area is 7.47×7.54 cm. Silver-coated hollow glass spheres with a density of 1300 kg/m^3 and an average diameter of $15 \text{ }\mu\text{m}$ are used as seed particles. Synchronization of the laser and camera, image processing, and acquisition of towing carriage speed (U_c) are enabled with the Dantec PIV 2000 processor. The towing tank is 100 m long and 3.05 m wide and deep. The geometry of interest is a flat plate of length $L = 1.2$ m. The plate is 0.5 m wide, 12.7 mm thick, and is equipped with a radiused leading edge and a tapered trailing edge. To initiate transition to turbulent flow, a row of cylindrical studs 0.8 mm high and 3.2 mm in diameter are fixed with 9.5 mm spacing on the plate at $x/L = 0.05$. The size and spacing of the studs is in accordance with standard practices. PIV measurements are made on the port side of the

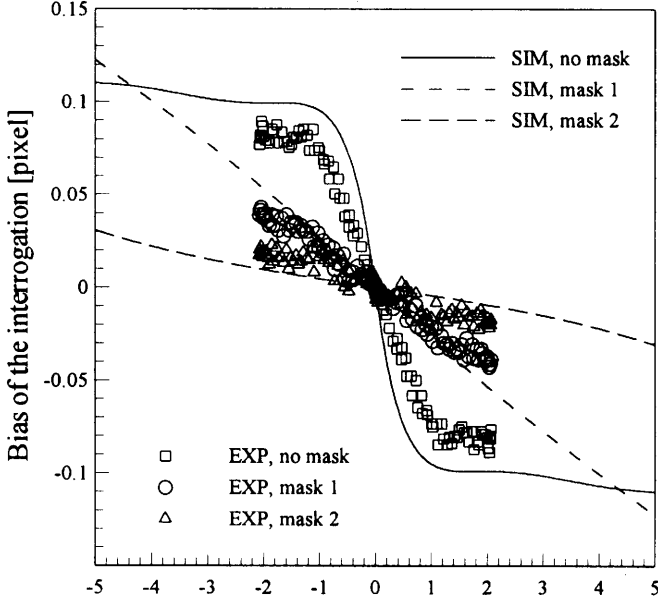
wake symmetry plane ($y = 0$). A right-handed Cartesian coordinate system is used with the origin at the intersection of the undisturbed free surface and leading edge ($x = 0$) of the plate. The (x, y, z) axes are directed downstream, transversely to starboard and upward, respectively. The plate is rigidly fixed to the carriage with 30.5 cm of draft and towed at a Froude number (Fr) of $Fr = 0.4$. The carriage speed is $U_c = 1.37$ m/s and the Reynolds number (Re) = 1.6×10^6 . At this towing speed, a 30-s window of data acquisition is available. The PIV system acquires vector maps at a rate of 7.5 Hz and produces roughly 200 vector maps per carriage run. The wake ($x/L = 1.25$, $-0.04 > y/L > 0.01$, $z/L = -0.0833$) is the region of interest, and the mean velocity components and Reynolds stresses are mapped by taking measurements in the xz and xy planes through manipulation of the light sheet plane and camera. Each variable is the result of statistical analyses of many (1000–2000) instantaneous measurement samples followed by normalization with U_c for velocities and with U_c^2 for Reynolds stresses. For convenience, the following discussions are restricted to the xy -plane measurements; however, the results and discussions can easily be extended to xz -plane data. For testing the evaluation algorithms, eight carriage runs are made with the xy -configuration of the PIV system, and 1035 PIV digital recording pairs are obtained. The time interval Δt between the two images in a PIV recording pair is set to $650 \text{ }\mu\text{s}$, which results in particle image displacement of 8–12 pixels.

For demonstrating the performance level of the evaluation algorithms, simulations of PIV recordings are used in which the position, size, and brightness of the particle images are determined with random number distributions. In the simulations, the particle images are assumed to have a Gaussian gray value distribution. The diameter of the particle images is between 2 and 4 pixels, and the brightness (gray value) is in the range of 60–250. A random noise level of gray value 50 is also included in the simulated PIV recordings. A series of simulation recording pairs are generated with an average particle distribution density of 20 in a 32×32 -pixel interrogation window and with particle image displacements from -5 to 5 pixels.

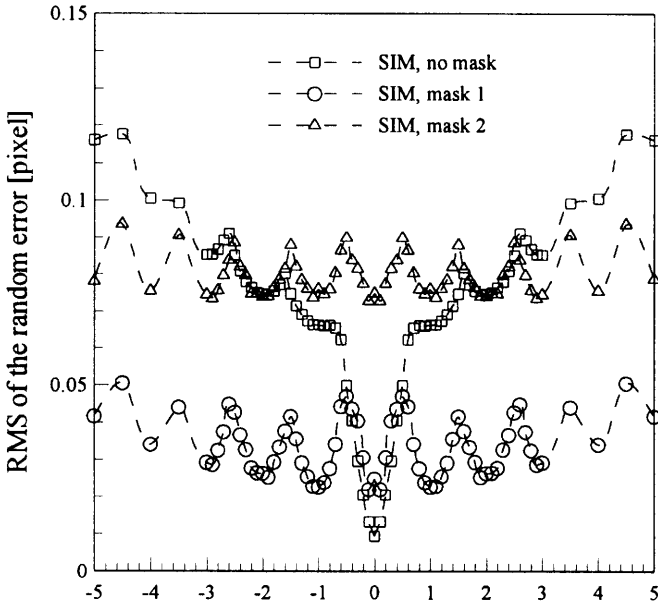
3

Bias and random errors of the evaluation algorithms

The experimental and simulated PIV recording pairs are evaluated with a 32×32 -pixel interrogation window by using the original correlation-based interrogation algorithm (no mask), the masked algorithm with Φ_1 (mask 1), and the masked algorithm with Φ_2 (mask 2). The dependency of the evaluation biases on the particle image displacement are shown in Fig. 1a, where the lines and symbols are results of the simulated (SIM) and experimental (EXP) PIV recording pairs, respectively. The benchmark particle image displacements for the experimental data (horizontal coordinate) are determined by the MQD method, which has been shown to have no bias error (Gui et al. 1998; Gui and Merzkirch 2000). Figure 1b shows the random evaluation errors of the three correlation-based algorithms at different particle image displacements by using simulated PIV recording pairs. A three-point



(a) Particle image displacement [pixel]



(b) Particle image displacement [pixel]

Fig. 1a, b. Bias and random error distributions of the correlation interrogation with and without Gaussian window masks: a bias error; b random error

Gaussian curve fit is used for determining sub-pixel displacements.

In summary, Fig. 1a shows that the absolute value of the evaluation bias for the original correlation-based interrogation algorithm is very small for particle displacements near zero and very large when the amplitude of the particle image displacement is more than 1 pixel. In the displacement range of $[-1,1]$, there is a large negative gradient of the evaluation bias. When window masks are used, both the absolute value and the gradient of the evaluation bias are reduced if the amplitude of the particle image displacement is not large (<4 pixels). The second window

mask is more effective than the first window mask for reducing the evaluation bias. However, the first window mask is more effective at reducing the random evaluation error in the tested particle displacement range (Fig. 1b).

4

Biases of turbulent flow measurement with PIV

For the xy -plane measurements, the mean velocity components (U , V) and Reynolds stresses (\overline{uu} , \overline{vv} , \overline{uv}) are obtained with the following data-reduction equations

$$U = \lim_{N \rightarrow \infty} \frac{1}{N} \sum_{i=1}^N U_i, \quad V = \lim_{N \rightarrow \infty} \frac{1}{N} \sum_{i=1}^N V_i$$

$$\overline{uu} = \lim_{N \rightarrow \infty} \frac{1}{N} \sum_{i=1}^N (U_i - U)^2, \quad \overline{vv} = \lim_{N \rightarrow \infty} \frac{1}{N} \sum_{i=1}^N (V_i - V)^2$$

$$\overline{uv} = \lim_{N \rightarrow \infty} \frac{1}{N} \sum_{i=1}^N (U_i - U) \cdot (V_i - V) \quad (4)$$

where N is the number of valid vectors at each evaluation point and the instantaneous velocity components (U_i , V_i) are determined with

$$U_i = \lambda S_{xi}, \quad V_i = \lambda S_{yi} \quad \text{with} \quad \lambda = \frac{L_{\text{obj}}}{L_{\text{img}} \cdot \Delta t \cdot U_c} \quad (5)$$

In Eq. (5), L_{obj} is the width of the camera view in the object plane, L_{img} is the width (pixels) of the CCD sensor, Δt is the time interval of the PIV recording pair, and (S_{xi}, S_{yi}) are the (x, y) components, respectively, of the particle image displacement obtained by evaluating the digital PIV recordings. The mean-velocity components (U , V) are functions of the mean particle displacements (S_x , S_y), respectively.

$$U = \lambda \lim_{N \rightarrow \infty} \frac{1}{N} \sum_{i=1}^N S_{xi} = \lambda S_x, \quad V = \lambda S_y \quad (6)$$

The bias errors of the mean velocity components (β_x , β_y) are related to the elementary bias errors with the following equations

$$\beta_x = \frac{\partial U}{\partial \lambda} \beta_\lambda + \frac{\partial U}{\partial S_x} \beta_{sx} = S_x \beta_\lambda + \lambda \beta_{sx} = \left(\frac{\beta_\lambda}{\lambda} + \frac{\beta_{sx}}{S_x} \right) U$$

$$\beta_y = \frac{\partial V}{\partial \lambda} \beta_\lambda + \frac{\partial V}{\partial S_y} \beta_{sy} = S_y \beta_\lambda + \lambda \beta_{sy} = \left(\frac{\beta_\lambda}{\lambda} + \frac{\beta_{sy}}{S_y} \right) V \quad (7)$$

where β_λ is the bias error for determining λ , and β_{sx} , β_{sy} are bias errors of the displacement components for the x and y axes, respectively.

The bias errors of the Reynolds stresses can be determined through a statistical analysis. An initial assumption is that the measured instantaneous velocity (U_i , V_i) is a sum of the true value (U_i^0 , V_i^0), the bias error ($\beta_{x,i}$, $\beta_{y,i}$), and the random error ($\varepsilon_{x,i}$, $\varepsilon_{y,i}$) as given by the following equations

$$U_i = U_i^0 + \beta_{x,i} + \varepsilon_{x,i}, \quad V_i = V_i^0 + \beta_{y,i} + \varepsilon_{y,i} \quad (8)$$

and the true mean velocity components and true Reynolds stresses are defined as

$$\begin{aligned} U_0 &= \lim_{N \rightarrow \infty} \frac{1}{N} \sum_{i=1}^N U_i^0, V_0 = \lim_{N \rightarrow \infty} \frac{1}{N} \sum_{i=1}^N V_i^0, \\ \overline{u_0 u_0} &= \lim_{N \rightarrow \infty} \frac{1}{N} \sum_{i=1}^N (U_i^0 - U_0)^2, \\ \overline{v_0 v_0} &= \lim_{N \rightarrow \infty} \frac{1}{N} \sum_{i=1}^N (V_i^0 - V_0)^2, \\ \overline{u_0 v_0} &= \lim_{N \rightarrow \infty} \frac{1}{N} \sum_{i=1}^N (U_i^0 - U_0) \cdot (V_i^0 - V_0) \end{aligned} \quad (9)$$

The mean bias errors can be expressed as functions of the true mean velocities, i.e., $\beta_x(U_0)$ and $\beta_y(V_0)$. When the fluctuation of the velocity is relatively small, the biases of the instantaneous flow can be determined with equations

$$\beta_{x,i} \approx \beta_x + \tau_x (U_i^0 - U_0), \quad \beta_{y,i} \approx \beta_y + \tau_y (V_i^0 - V_0) \quad (10)$$

where $\tau_x (=d\beta_x/dU_0)$ and $\tau_y (=d\beta_y/dV_0)$ are gradients of the mean velocity biases. According to the definitions in Eqs. (4) and (9) and the approximation in Eq. (10), the measured and true normal stress in the x direction are related by

$$\begin{aligned} \overline{uu} &= (1 + \tau_x)^2 \overline{u_0 u_0} + \lim_{N \rightarrow \infty} \frac{1}{N} \sum_{i=1}^N \varepsilon_{x,i}^2 + 2(1 + \tau_x) \\ &\quad \times \lim_{N \rightarrow \infty} \frac{1}{N} \sum_{i=1}^N \varepsilon_{x,i} (U_i^0 - U_0) \end{aligned} \quad (11)$$

The third term on the right-hand side of Eq. (11) is the sum of the product of two independent random values, which have a mean of zero, and as such, can be neglected. The resulting expression is

$$\overline{uu} = (1 + \tau_x)^2 \overline{u_0 u_0} + \varepsilon_x^2 \quad (12)$$

In the same way the following relations can also be formulated

$$\overline{vv} = (1 + \tau_y)^2 \overline{v_0 v_0} + \varepsilon_y^2, \quad \overline{uv} = (1 + \tau_x)(1 + \tau_y) \overline{u_0 v_0} \quad (13)$$

Here $\varepsilon_x, \varepsilon_y$ are root-mean-square (RMS) values of the random errors of the two velocity components. The biases for the Reynolds stresses can then be determined:

$$\begin{aligned} \beta_{uu} &= \overline{uu} - \overline{u_0 u_0} = \overline{uu} - \frac{\overline{uu} - \varepsilon_x^2}{(1 + \tau_x)^2} \approx \frac{2\tau_x \overline{uu} + \varepsilon_x^2}{(1 + \tau_x)^2} \\ \beta_{vv} &= \overline{vv} - \overline{v_0 v_0} = \overline{vv} - \frac{\overline{vv} - \varepsilon_y^2}{(1 + \tau_y)^2} \approx \frac{2\tau_y \overline{vv} + \varepsilon_y^2}{(1 + \tau_y)^2} \\ \beta_{uv} &= \overline{uv} \left(1 - \frac{1}{(1 + \tau_x)(1 + \tau_y)} \right) \approx \frac{\tau_x + \tau_y}{(1 + \tau_x)(1 + \tau_y)} \overline{uv} \end{aligned} \quad (14)$$

Equation (14) shows that the bias error in the normal stresses is a function of the random error and the gradi-

ents of the mean velocity biases, whereas the bias error for the shear stress component is only a function of the gradients of the mean velocity biases. In order to determine the bias error of the Reynolds stresses, the bias gradients of the mean velocity components must be known.

According to Fig. 1a, the bias for determining the particle image displacement (β_{sx}, β_{sy}) is a function of the true displacement (S_{x0}, S_{y0}). From Eq. (7) and the following expression ($S_x = S_{x0} + \beta_{sx}$)

$$\begin{aligned} \frac{d\beta_x}{dS_{x0}} &= \frac{d}{dS_{x0}} [(S_{x0} + \beta_{sx})\beta_\lambda + \lambda\beta_{sx}] \approx \frac{d}{dS_{x0}} (S_{x0}\beta_\lambda + \lambda\beta_{sx}) \\ &= \beta_\lambda + \lambda \frac{d\beta_{sx}}{dS_{x0}} = \beta_\lambda + \lambda\tau_{sx} \end{aligned} \quad (15)$$

where $\tau_{sx} (=d\beta_{sx}/dS_{x0})$ is the gradient of the evaluation bias β_{sx} . From the expression ($U = U_0 + \beta_x$) and Eqs. (6) and (15)

$$\begin{aligned} \frac{dU_0}{dS_{x0}} &= \frac{d}{dS_{x0}} (U - \beta_x) = \frac{d}{dS_{x0}} [\lambda(S_{x0} + \beta_{sx}) - \beta_x] \\ &= \lambda \left(1 + \frac{d\beta_{sx}}{dS_{x0}} \right) - \frac{d\beta}{dS_{x0}} = \lambda(1 + \tau_{sx}) - \frac{d\beta_x}{dS_{x0}} = \lambda - \beta_\lambda \end{aligned} \quad (16)$$

The mean velocity bias gradient τ_x can be determined as

$$\tau_x = \frac{d\beta_x}{dU_0} = \frac{d\beta_x}{dS_{x0}} \bigg/ \frac{dU_0}{dS_{x0}} = \frac{\tau_\lambda + \tau_{sx}}{1 - \tau_\lambda} \quad (17)$$

where $\tau_\lambda = \beta_\lambda/\lambda$. Similarly, τ_y can be formulated as

$$\tau_y = \frac{\tau_\lambda + \tau_{sy}}{1 - \tau_\lambda} \quad (18)$$

with $\tau_{sy} = d\beta_{sy}/dS_{y0}$.

Note that, in the above discussions, the number of measurement samples is unlimited. Furthermore, several PIV error sources that are independent of the evaluation bias and not central to the present discussions are not considered, e.g., position (translational and rotational) biases of the laser sheet, optical (lens) biases, and biases incurred from particle density differences from the towing tank water.

5

Influences of the evaluation bias on the measurements

The relationship between the evaluation bias error and the bias error of the mean velocity components is described in Eq. (7) as a linear function, i.e., the measurement of the mean velocity component is directly influenced by the evaluation bias magnitude. When the original correlation-based interrogation algorithm is used, low evaluation bias error can only be achieved with very small particle displacements. However, the dynamic range of the evaluation can effectively be increased with the digital window masks (see Fig. 1a). Because the evaluation errors of the masked correlation algorithms are also significant in regions of large particle image displacements, an artificial offset of the interrogation window is necessary for reducing the particle image displacement.

The bias errors of the Reynolds stresses are not directly influenced by the evaluation bias magnitude. However, as

shown in Eqs. (14), (17), and (18), they are influenced by the evaluation bias gradient. Here, the discussions begin with the effects of the evaluation bias on the shear stress, because they are not influenced by the random error. If we assume $\beta_\lambda = 0$, then the gradient of the mean velocity bias equals the gradient of the evaluation bias and τ_x, τ_y in Eq. (14) can be replaced by τ_{sx}, τ_{sy} , respectively. Because the evaluation bias gradient of the correlation-based interrogation algorithm is in the range $-1 < \tau_s < 0$ ($\tau_s = \tau_{sx}, \tau_{sy}$), the bias of the shear stress has an opposite sign. This means that the evaluation bias causes a reduction in the amplitude of the shear stress. In order to reduce the bias of the shear stress, the absolute value of the evaluation bias gradient should be minimized. When using the original correlation algorithm the evaluation bias is a minimum, i.e., $\beta_s \approx 0$ ($\beta_s = \beta_{sx}, \beta_{sy}$), if the particle image displacement to be determined is zero pixel, however, the gradient of the evaluation bias is a maximum at zero displacement ($\tau_s \approx -0.08$). Therefore, the measurement of the mean velocity and the Reynolds stress cannot be improved at the same time by only using the window offset. To demonstrate this, the original correlation algorithm (without window mask) is used for evaluating the 1,035 PIV recording pairs taken in the wake of the vertical surface-piercing flat plate at $x/L = 1.25$ and $z/L = -0.0833$.

Without window offset, the mean particle image displacement in the x -direction is about 9 pixels at the wake center ($y = 0$), 12 pixels far from the wake center ($y/L = -0.04 \sim -0.025$), and 10 pixels at the position of maximum turbulence ($y/L = -0.01$). The overall mean particle displacement in the y direction is nearly 0 pixel. A window offset includes artificial shifts of the interrogation window in the two coordinate directions and is defined here as (x -offset, y -offset). Four window offsets of (10, 0), (10, 2), (12, 0) and (12, 2) pixels are chosen for the correlation interrogation, so that the particle image displacements to be evaluated (S_x, S_y) at $y/L = -0.01$ are roughly (0, 0), (0, -2), (-2, 0), and (-2, -2) pixels, respectively. Far from the wake center, the particle displacements are about (-2, 0), (-2, -2), (0, 0), and (0, -2) pixels. A performance benchmark is established by evaluation of these PIV recordings using the MQD method.

The shear stress distributions of the original correlation algorithm using different window offsets are shown in Fig. 2, and also include the results of the MQD method. The evaluation bias of the original correlation algorithm with window offset (12, 2) is relatively large at $y = -0.01$, because the particle displacement is about (-2, -2) pixels (see Fig. 1a). However, Fig. 2 does not show obvious differences between the shear stress obtained with the MQD method and that obtained with the original correlation algorithm at this window offset. The reason is that the amplitude of the evaluation bias gradient is very small in both the x and y direction at the position of the maximum shear stress ($\tau_{sx} \approx 0$ and $\tau_{sy} \approx 0$ at $y/L = -0.01$). Nevertheless, the largest difference in the shear stress distribution is shown between the MQD method and the correlation algorithm with window offset of (10, 0) pixels. At this window offset, the particle displacement to be determined is (0, 0) pixels at $y/L = -0.01$ and the negative

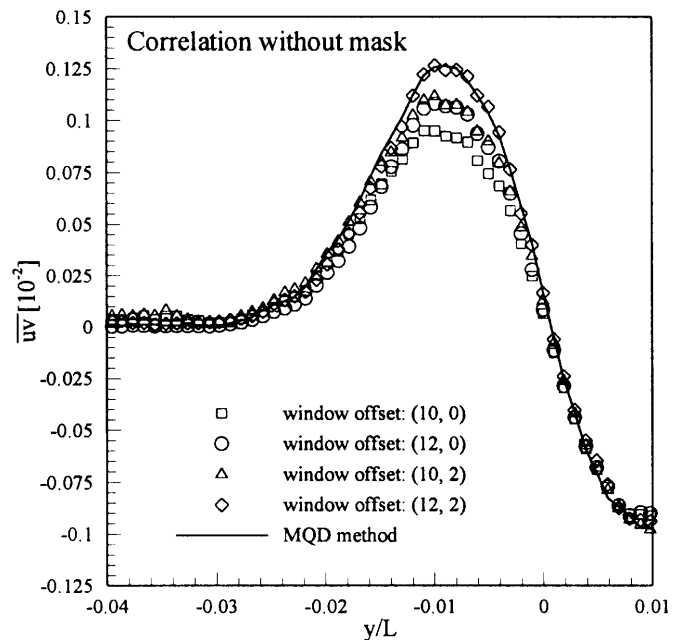
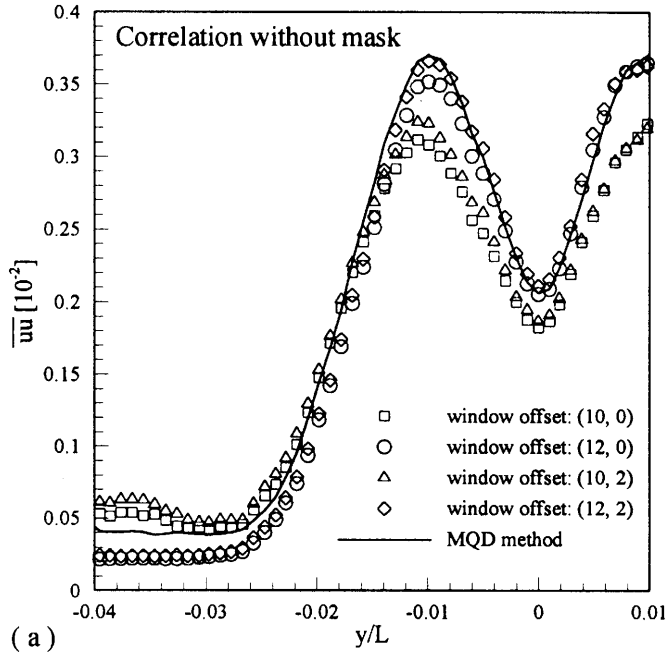


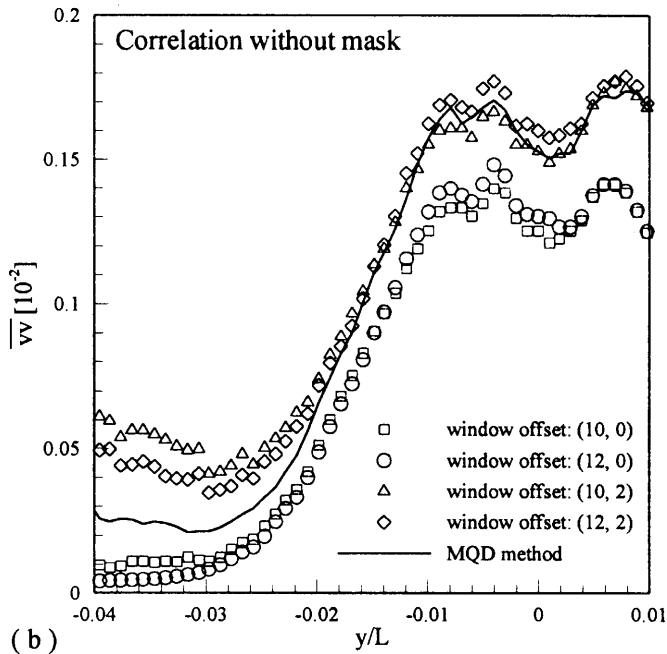
Fig. 2. Shear stress distributions resulting from the correlation interrogation without mask

gradient of the evaluation bias is maximum in both directions ($\tau_{sx} \approx -0.08$, $\tau_{sy} \approx -0.08$). The shear stress distributions of window offsets (10, 2) and (12, 0) fall between those of window offsets (10, 0) and (12, 2). The reason is that the negative bias gradient with these two window offsets is large in one direction and small in the other direction ($\tau_{sx} \approx -0.08$, $\tau_{sy} \approx 0.0$ and $\tau_{sx} \approx 0$, $\tau_{sy} \approx -0.08$, respectively). Similar influences of the interrogation bias can be shown on the measurements of normal stresses (see Fig. 3). The normal stress along a given coordinate is principally influenced by the window offset in the same coordinate direction. The window offset in another direction does not change the evaluation bias gradient in the given direction but does make changes in the random evaluation error. Therefore, it also affects the normal stress measurement, which can be seen in Fig. 3b for $\overline{v^2}$ distributions with window offset (10, 2) and (12, 2) between $y/L = -0.04$ and -0.02 .

Simulations and experiments in Fig. 1a show that the large gradient of the evaluation bias of the correlation-based interrogation algorithm near zero displacement can be avoided by using the Gaussian window masks. Together with the window-offset technique, the window masks enable both the evaluation bias and the bias gradient to be minimal at zero displacement. The dependencies of the evaluation errors on the particle image displacement can also be reduced when using the window masks. The effects of the window masks are also demonstrated here by using the PIV recordings discussed above. Figure 4 shows the shear stress distributions and the distributions of one of the normal stresses across the wake by using two types of window masks and four window offsets. In comparison with Figs. 2 and 3, the biases of the Reynolds stress are effectively reduced. The influence of the window offset is no longer apparent. The second window mask seems more effective for reducing the measurement bias of the shear



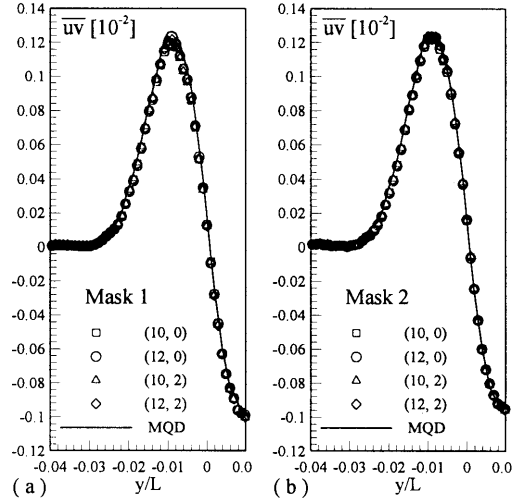
(a)



(b)

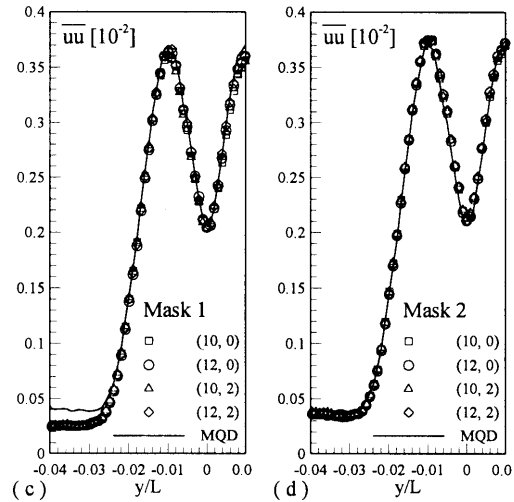
Fig. 3a, b. Normal stress distributions resulting from the correlation interrogation without mask: a distribution of \overline{uu} ; b distribution of \overline{vv}

stress than for the first window mask. In Fig. 4c and d in the range of $-0.04 < y/L < -0.025$, the normal stress obtained with the first window mask is lower than that obtained with the second window mask. This can be explained, as shown in Fig. 1b, by the fact that the first mask produces less random error than the second one. Since the experimentally determined normal stress includes not only the real value but also the random measurement error, the uncertainty is relatively high when measuring the normal stress of the low turbulence flow.



(a)

(b)



(c)

(d)

Fig. 4a-d. Reynolds stress distributions resulting from the masked correlation interrogation algorithms: a shear stress distribution resulting from the first window mask; b shear stress distribution resulting from the second window mask; c normal stress distribution resulting from the first window mask; d normal stress distribution resulting from the second window mask

6 Contributions to uncertainty reduction

In order to demonstrate the effect of the window masks on the total uncertainty of the PIV measurements, an uncertainty assessment is conducted for the example in Sect. 5 using a 95% confidence large-sample approach recommended by the AIAA for the vast majority of engineering tests (AIAA Standard 1995). The approach is derived and explained in detail by Coleman and Steele (1995).

The uncertainty (U_X) of a measurement result (X) is expressed as a root-sum-square (RSS) of the bias (B_X) and precision (P_X) limits

$$U_X = \sqrt{B_X^2 + P_X^2} \quad (19)$$

The bias limits of the mean velocity components can be determined with the RSS method as

$$B_U = \sqrt{(S_x B_\lambda)^2 + (\lambda B_s)^2}, \quad B_V = \sqrt{(S_y B_\lambda)^2 + (\lambda B_s)^2} \quad (20)$$

where B_λ and B_s are bias limits for factor λ and for the evaluated particle image displacement S , respectively. The bias limits of the Reynolds stresses are here assumed to be asymmetric, and they are determined by identifying the maximum and minimum values of the possibilities according to Eq. (14)

$$B_{uu}^+ = \frac{-2\tau_{x,\min}\overline{uu} - \varepsilon_x^2}{(1 + \tau_{x,\min})^2}, \quad B_{uu}^- = \frac{2\tau_{x,\max}\overline{uu} + \varepsilon_x^2}{(1 + \tau_{x,\max})^2}$$

$$B_{vv}^+ = \frac{-2\tau_{y,\min}\overline{vv} - \varepsilon_y^2}{(1 + \tau_{y,\min})^2}, \quad B_{vv}^- = \frac{2\tau_{y,\max}\overline{vv} + \varepsilon_y^2}{(1 + \tau_{y,\max})^2}$$

$$\begin{cases} B_{uv}^+ = -\frac{\tau_{x,\min} + \tau_{y,\min}}{(1 + \tau_{x,\min})(1 + \tau_{y,\min})}\overline{uv} & \text{for } \overline{uv} \geq 0 \\ B_{uv}^+ = -\frac{\tau_{x,\max} + \tau_{y,\max}}{(1 + \tau_{x,\max})(1 + \tau_{y,\max})}\overline{uv} & \text{for } \overline{uv} < 0 \end{cases}$$

$$\begin{cases} B_{uv}^- = \frac{\tau_{x,\max} + \tau_{y,\max}}{(1 + \tau_{x,\max})(1 + \tau_{y,\max})}\overline{uv} & \text{for } \overline{uv} \geq 0 \\ B_{uv}^- = \frac{\tau_{x,\min} + \tau_{y,\min}}{(1 + \tau_{x,\min})(1 + \tau_{y,\min})}\overline{uv} & \text{for } \overline{uv} < 0 \end{cases} \quad (21)$$

where $\tau_{x,\min}$, $\tau_{y,\min}$ and $\tau_{x,\max}$, $\tau_{y,\max}$ are the minimum and maximum values of the bias gradients of the mean velocity components (U , V), respectively. They are determined according to Eqs. (17) and (18) with $\beta_\lambda = \pm B_\lambda$ and with the minimum and maximum of the evaluation bias gradient ($\tau_{s,\min}$, $\tau_{s,\max}$). Since the bias limits B_λ^\pm are defined as non-negative values, a bias limit is set to zero when the calculated value from Eq. (21) is negative.

The precision limit for multiple tests of the measured variable X is given by

$$P_X = \frac{K \cdot St_X}{\sqrt{M}} \quad (22)$$

where K is the coverage factor and equals 2 for a 95% confidence level, and St_X is the standard deviation of the sample of M readings (here $M = N = 1,035$).

For the current example, the factor λ has a value of 0.0803 m/s. pixel, and the bias limit is estimated as $B_\lambda = 3.373 \times 10^{-4}$ m/s. pixel. When using the original correlation interrogation, the evaluation bias limit B_s can be chosen as 0.1 pixel, and the minimum and maximum bias gradient can be estimated as $\tau_{s,\min} = -0.08$ and $\tau_{s,\max} = 0$. For the correlation interrogation with mask 1, the evaluation bias limit is $B_s = 0.05$ pixel, and $\tau_{s,\min}$, $\tau_{s,\max}$ are -0.025 and 0, respectively. For mask 2, the bias limit is 0.025 pixel, and the maximum of the bias gradient is $\tau_{s,\min} = -0.01$. The random system noise level can be established through uniform-flow tests, i.e., no model.

For demonstrating the contributions of the window masks to the uncertainty reduction, the bias limits are compared with the precision limits. In Fig. 5, the distributions of the bias and precision limits of the mean velocity component U by using the original and masked correlation interrogation algorithm (mask 1) are illu-

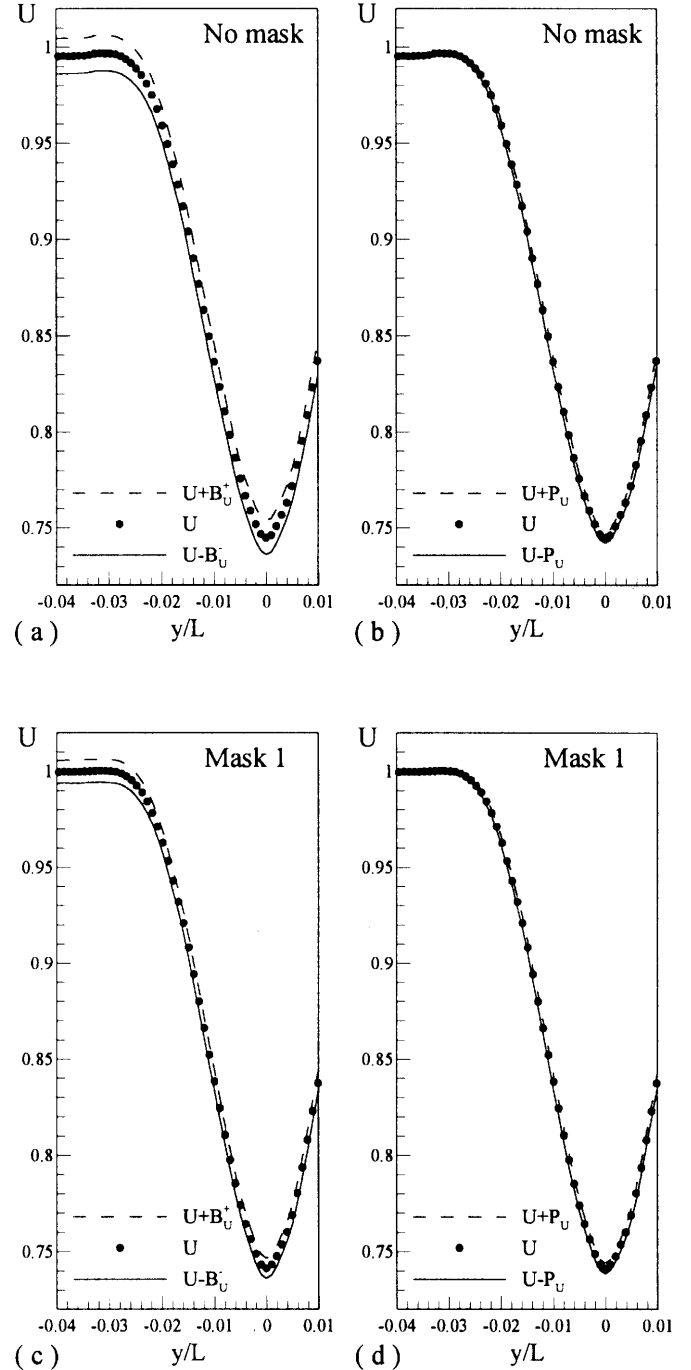


Fig. 5a-d. Bias and precision limits of U resulting from the correlation interrogation with and without Gaussian window mask: a bias limit without window mask; b precision limit without window mask; c bias limit with the first window mask; d precision limit with the first window mask

strated with error bands. The bias limit of the mean velocity is obviously smaller when using the window mask. In comparison with the bias limits, the precision limits with and without window mask are both very small. This means the bias error is the main source of the measurement uncertainty of the mean velocity component U . The bias and precision limit distributions of the shear stress are also shown in Fig. 6 with error bands. The improvement of the bias limits of the shear stress can be seen

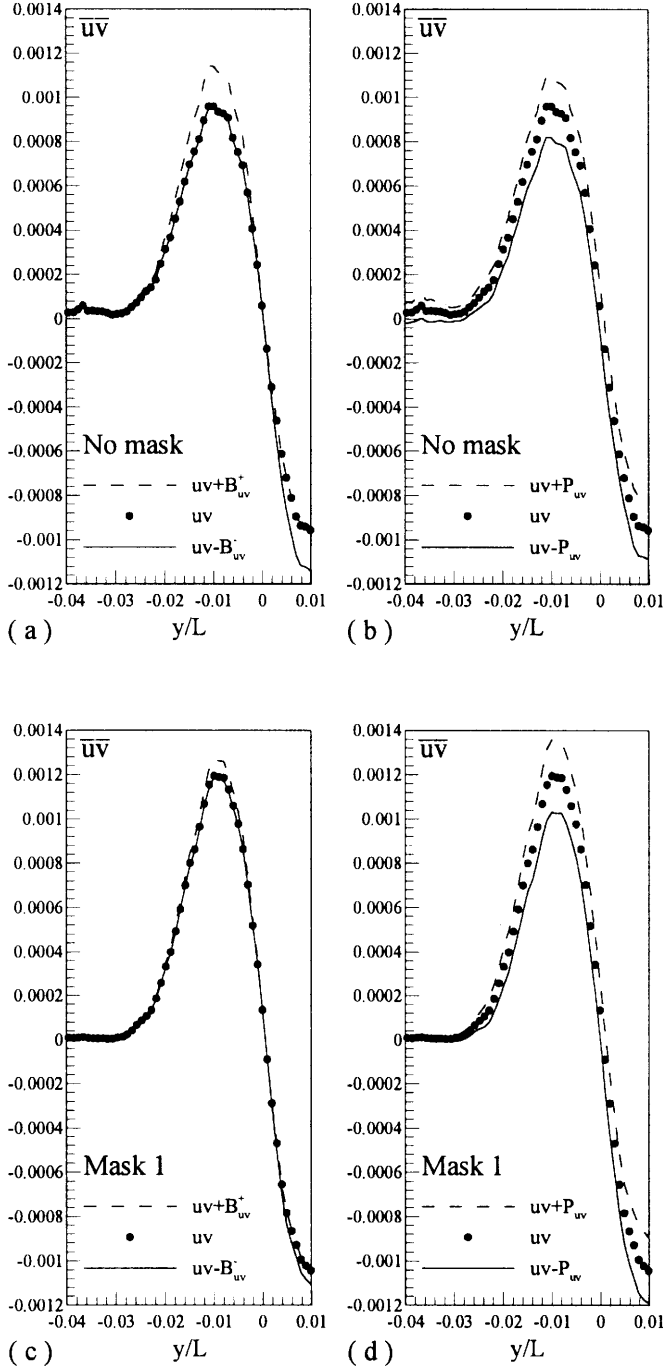


Fig. 6a-d. Bias and precision limit distributions of shear stress \overline{uv} : a bias limit without window mask; b precision limit without window mask; c bias limit with the first window mask; d precision limit with the first window mask

clearly in Fig. 6a and c. The precision limit of the shear stress with the first window mask (Fig. 6b) appears larger than without the window mask (Fig. 6d). For a more detailed comparison, the bias and precision limits of the shear stress are normalized by the dynamic range of the shear stress $D_{uv} (=2.25 \times 10^{-3})$ and shown in Fig. 7 for the three algorithms. The bias limit of the shear stress (Fig. 7a) is effectively reduced with the two window masks, and the second window mask is more effective than the first. Figure 7b shows that the precision limit with the second

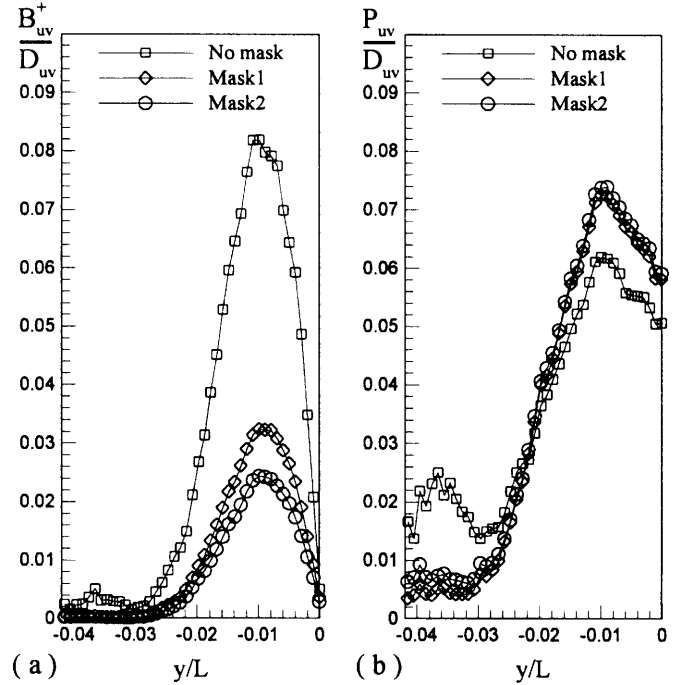


Fig. 7a-b. Bias and precision limits of shear stress \overline{uv} with dynamic range D_{uv} using different algorithms. a upper bias limits; b precision limits

window mask is higher than that with the first window mask, but the difference is very small. In the high turbulence region, the window masks may enlarge the precision limit of the shear stress measurement. This can be explained by the fact that the Gaussian mask reduces the effective area of the interrogation window. There are two methods to reduce the precision limit of the masked correlation interrogation algorithm: (1) increasing the size of the interrogation window or (2) increasing the number of measurement samples. Increasing the window size may reduce the spatial resolution of the measurement and increase the evaluation time. Therefore, the number of measurement samples will be increased for future PIV measurements in the IIHR towing tank.

7 Conclusions

The influences of the evaluation bias of the correlation-based interrogation algorithm on PIV measurement of turbulent flow were investigated. Experimental tests in the Iowa Institute of Hydraulic Research towing tank with a towed PIV system and a surface-piercing flat plate and simulations demonstrated that the measured mean velocity and Reynolds stress components are affected by the evaluation bias and the gradient of the evaluation bias, respectively.

The evaluation bias of the original (unmasked) correlation-based interrogation algorithm is dependent on the particle image displacement. The bias is small at zero displacement but becomes large when the displacement is greater than 1 pixel. The evaluation bias gradient is a maximum at zero displacement and becomes small when the displacement is greater than 1 pixel. Therefore, the

measurement of the mean velocity and Reynolds stresses cannot be improved at the same time by only using the window-offset technique. Further investigation demonstrates that the large gradient of the evaluation bias of the original correlation-based interrogation algorithm near zero displacement can be avoided by using the Gaussian window masks. Together with the window-offset technique, the window masks enable both the evaluation bias and the bias gradient to be minimized. The dependence of the evaluation errors on the particle image displacement can also be reduced when using the window masks. Between the two window masks tested, the second window mask is more effective for reducing the evaluation bias and the gradient, but the first window mask is more capable of reducing the random evaluation error.

A standard uncertainty assessment of the experimental data shows that, for the current test case, the bias error of the mean velocity is the main source of the measurement uncertainty and can be reduced by using the window masks. The bias error of the Reynolds stress may be very large at the position of peak turbulence when using the original correlation-based interrogation algorithm, and it can also effectively be reduced by using the window masks. For further reduction of the Reynolds stress measurement uncertainty, the number of measurement samples should be increased.

The results herein will be used for quality assurance in future IIHR towing tank PIV studies. One such study includes mean and turbulence measurements in the flow field of David Taylor Model Basin (DTMB) model 5512 in regular head waves for validation of unsteady Reynolds-averaged Navier–Stokes (RANS) codes. The other study involves mean and turbulence measurements in the flow field of a surface-piercing flat plate traveling with a stationary Stokes wave for turbulence modeling.

References

- Adrian RJ** (1988) Statistical properties of particle image velocimetry measurements in turbulent flow. In: Adrian RJ, et al (ed) *Laser anemometry in fluid mechanics*. Instituto Superior Tecnico, Lisbon, pp 115–129
- Adrian RJ** (1991) Particle-imaging techniques for experimental fluid mechanics. *Annu Rev Fluid Mech* 23: 261–304
- AIAA Standard (1995) Assessment of wind tunnel data uncertainty. AIAA S-071-1995, Washington, DC
- Cenedese A; Paglialunga A** (1990) Digital direct analysis of a multiexposed photograph in PIV. *Exp Fluids* 8: 273–280
- Coleman HW; Steele WG** (1995) Engineering application of experimental uncertainty analysis, *AIAA J* 33: 1888–1896
- Fincham AM; Spedding GR** (1997) Low cost, high resolution DPIV for measurement of turbulent fluid flow. *Exp Fluids* 23: 449–462
- Freek C; Wüste A; Hentschel W** (1996) A novel diode laser PIV/PTV system for the investigation of intake flows in i.c. engines. 8th Int Symp on Applications of Laser Techniques to Fluid Mechanics, 8–11 July, Lisbon, Portugal
- Freek C; Sousa JMM; Hentschel W; Merzkirch W** (1999) Digital image compression PIV, a tool for IC-engine research. *Exp Fluids* 27: 310–320
- Gui L; Merzkirch W** (1996) A method of tracking ensembles of particle images. *Exp Fluids* 21: 465–468
- Gui L; Merzkirch W** (2000) A comparative study of the MQD method and several correlation-based PIV evaluation algorithms. *Exp Fluids* 28: 36–44
- Gui L; Merzkirch W; Lindken R** (1998) An advanced MQD tracking algorithm for DPIV. 9th Int Symp on Applications of Laser Techniques to Fluid Mechanics, 13–16 July, Lisbon, Portugal
- Gui L; Longo J; Stern F** (1999) Towing tank PIV measurement system and data and uncertainty assessment for DTMB model 5512. 3rd Int Workshop on Particle Image Velocimetry, 16–18 Sept., Santa Barbara, Calif.
- Gui L; Merzkirch W; Fei R** (2000) A digital mask technique for reducing the bias error of the correlation-based PIV interrogation algorithm. *Exp Fluids* (in press)
- Huang HT; Fiedler HE; Wang JJ** (1993) Limitation and improvement of PIV – Part I: limitation of conventional techniques due to deformation of particle image patterns. *Exp Fluids* 15: 168–174
- Kemmerich Th; Rath HJ** (1994) Multi-level convolution filtering technique for digital laser-speckle-velocimetry. *Exp Fluids* 17: 315–322
- Liu Z-C; Landreth CC; Adrian RJ; Hanratty TJ** (1991) High resolution measurement of turbulent structure in a channel with particle image velocimetry, *Exp Fluids* 10: 301–312
- Raffel M; Willert CE; Kompenhans J** (1997) *Particle image velocimetry – a practical guide*. Springer-Verlag, Berlin Heidelberg New York
- Ronneberger O; Raffel M; Kompenhans J** (1998) Advanced evaluation algorithm for standard and dual plane particle image velocimetry. 9th Int Symp on Applications of Laser Techniques to Fluid Mechanics, 13–16 July, Lisbon, Portugal
- Schlueter Th; Merzkirch W** (1996) PIV measurements of the time-averaged flow velocity downstream of flow conditioners in a pipeline. *Flow Meas Instrum* 7: 173–179
- Westerweel J; Draad AA; Hoeven JGTh; Oord J** (1996) Measurement of fully-developed turbulent pipe flow with digital particle image velocimetry. *Exp Fluids* 20: 165–177
- Westerweel J** (1997) Fundamentals of digital particle image velocimetry. *Meas Sci Technol* 8: 1379–1393
- Westerweel J; Dabiri D; Gharib M** (1997) The effect of a discrete window offset on the accuracy of cross-correlation analysis of digital PIV recordings, *Exp Fluids* 23: 20–28
- Willert C** (1996) The fully digital evaluation of photographic PIV recordings. *Appl Sci Res* 56: 79–102
- Willert CE; Gharib M** (1991) Digital particle image velocimetry. *Exp Fluids* 10: 181–193
- Xiong W; Merzkirch W** (1997) DPIV experiments on turbulent pipe flow. Proc 7th Int Conf on Laser Anemometry Advances and Applications, pp 475–482